Publication I

Arttu Polojärvi and Jukka Tuhkuri. 3D discrete numerical modeling of ridge keel punch through tests. ***Cold Regions Science and Technology*****, 56, 18-29, 2009.**

Cold Regions Science and Technology 56 (2009) 18–29

Contents lists available at ScienceDirect

Cold Regions Science and Technology

journal homepage: www.elsevier.com/locate/coldregions

3D discrete numerical modelling of ridge keel punch through tests

Arttu Polojärvi *, Jukka Tuhkuri

Helsinki University of Technology, Espoo, Finland

ARTICLE INFO

Article history:
Received 13 May 2008
Accepted 21 September 2008

Keywords:
Discrete element method
Ice ridges
Punch through test
Ice rubble
Modelling

ABSTRACT

Ridge keel punch through tests were simulated in 3D. In simulations unconsolidated ridge keel was modelled as a rubble pile of loose ice blocks. Combined finite–discrete element method (FEM–DEM) with rigid discrete elements representing ice blocks was used. Simulations were run in full scale. In total 47 simulations were run with various friction coefficients and keel depths. The failure process of simulated rubble piles was analysed and the shear strength of the rubble pile was derived from results. The effect of rubble porosity, keel depth and friction on shear strength of the pile was also analysed. The simulation results were compared to laboratory and full-scale punch through tests of unconsolidated ice rubble. Shear strength values achieved from simulations were in range for experimental results. Failure process was observed to be similar to laboratory experiments.

1. Introduction

Ice ridges are common and important features in Northern sea s. Ridges are formed by compression and shearing of sea ice driven by wind and currents. Ridge structure can be divided into three main parts. The visible part above the waterline and level ice is called sail. The sail is formed of ice blocks, snow and air. Close to the waterline lies the consolidated layer. It is a mixture of frozen water and ice blocks broken of ice sheets during the ridge formation. The consolidated layer forms after ridge formation, as the water in pores between ice blocks freeze. Under the consolidated layer lies a rubble pile of ice which can be extensive in size. This part is called the keel. The structure of the keel can vary from having a structure with several layers of rafted ice forming a layered structure, to a rubble with arbitrarily piled ice blocks. The keel can be unconsolidated, i.e. it can consist of loose ice blocks, or consist of ice blocks bonded together with cohesive bonds. Usually it has a mixture of loose ice blocks and blocks with cohesive bonds. Keel loads are a part of ridge loads on marine structures and vessels used in the winter navigation, and therefore research on the material properties of ice rubble is needed to enable safe design of these structures. Ice rubble properties have been experimentally studied using shear box tests, direct shear tests and punch through tests (Bruneau et al., 1998).

In a punch through test, a flat indentor is ran down into the ice rubble. From the dimensions of the test set up and measurements during the experiment some material properties for the rubble can be derived. The derivation of the material properties from the experimental data is not a straightforward task and usually requires numerical modelling (Liferov et al., 2003). Fig. 1 shows an example of a full-scale punch through test as conducted by Heinonen and Määttänen (2000, 2001b). In the figure, a circular indentor with diameter d is moved down into ice rubble with thickness h_k measured from the waterline. As only loads caused by the rubble are of interest, a cylindrical plug with height h_{cut} under the indentor is cut through the consolidated layer. Hence, the effective keel thickness becomes $h = h_k + FB - h_{cut}$, where FB is the free board. As one result, the force needed to move the indentor as a function of indentor displacement is achieved. Also in Fig. 1, a possible shear plane with an angle α from the vertical is presented.

First full-scale experiments on ridge keel properties using punch through tests were conducted by Leppäranta and Hakala (1992) in Baltic sea with loading platform and concrete blocks. Later more sophisticated equipment for measuring ice rubble strength was used, e.g. Bruneau et al. (1998) and Croasdale et al. (2001). Heinonen and Määttänen performed a series of tests during five winters (1998–2003) in the Baltic sea (Heinonen and Määttänen, 2000, 2001a,b; Heinonen, 2004). Heinonen (2004) used results from these tests to derive a constitutive law for a continuum model of the ice rubble. In his work he assumed that the peak load for the ice rubble is due to the breakage of the skeleton formed by the cohesive bonding between ice blocks within the rubble.

In addition to full scale experiments, laboratory scale punch through tests have also been performed (Leppäranta and Hakala, 1992; Bruneau et al., 1998; Azarnejad et al., 1999; Azarnejad and Brown, 2001; Jensen et al., 2001; Lemee and Brown, 2002). An important motivation for the laboratory tests is the need to understand the failure mechanisms of ice rubble. This understanding, in turn, is important when forming assumptions used in modelling. During field tests, underwater cameras and measurements on

* Corresponding author. Fax: +358 9 451 3449.
E-mail addresses: arttu.polojarvi@tkk.fi (A. Polojärvi), jukka.tuhkuri@tkk.fi (J. Tuhkuri).

0165-232X/$ – see front matter © 2008 Elsevier B.V. All rights reserved.
doi:10.1016/j.coldregions.2008.09.008

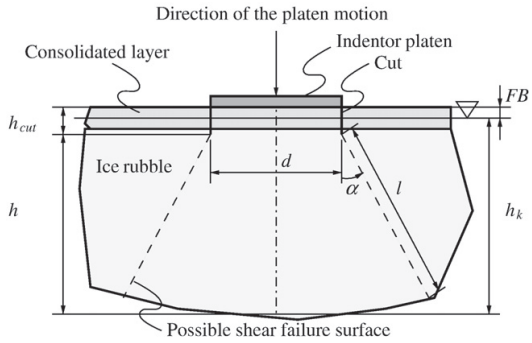

Fig. 1. Sketch of the punch through test (reproduced from Heinonen, 2004 with modifications). An indentor with diameter d is loading an ice rubble with average keel depths h_k measured from the waterline and h measured from the cut made through the consolidated layer. Depth of the cut is h_{cut}. *FB* is free board of the ice sheet. α is the angle and l is the slant height of an assumed failure surface.

displacements within the keel and keel bottom have been used (Croasdale et al., 2001; Heinonen, 2004), but in the field the possibility to observe actual failure mechanisms of ice rubble is rather limited. While results from laboratory tests have brought some understanding on the failure mechanisms, the laboratory tests have also lead to results that partly differ from field tests (Croasdale et al., 2001; Liferov and Bonnemaire, 2005).

Ice rubble has been modelled by soil mechanics models (Ettema and Urroz, 1989), continuum models (Heinonen and Määttänen, 2001a; Liferov et al., 2002, 2003; Heinonen, 2004), discrete models (Tuhkuri and Polojärvi, 2005) and pseudo-discrete models (Liferov, 2005). Reviews on both experimental work and modelling have been written by Liferov and Bonnemaire (2005) and Liferov (2005).

In the presented work, ice rubble is modelled as discontinuous media. When rubble is assumed to be discontinuous, the deformation of the rubble pile becomes modelled through displacements of the individual ice blocks within it. The ice blocks within the rubble pile are assumed to interact through pairwise contacts which cause motion of the blocks. Traditional way of modelling discontinuum is the discrete element method (DEM) first introduced by Cundall and Strack (1979). DEM has been used in various applications including material sciences, geophysics, rock mechanics, fracture mechanics and ice mechanics. In ice mechanics, DEM has been used, for example, in studies of ice ridging (Hopkins, 1992, 1998; Hopkins et al., 1999) and ice pile-up against inclined structures (Paavilainen et al., 2006). A two dimensional DEM has been used to model punch through tests (Tuhkuri and Polojärvi, 2005).

In the research presented in this article, punch through tests of unconsolidated ice rubble were modelled using combined finite–discrete element method (FEM–DEM) (Munjiza et al., 1995; Munjiza, 2004). This modelling technique was chosen as it gives robust platform for solving contacts between arbitrary shaped polyhedral blocks. Simulations were run in three dimensions using ice blocks with realistic sizes and shapes. In simulations discrete elements representing ice blocks were rigid. First a rubble pile of ice was generated. Then a simulation of a punch through test using the rubble was conducted. A series of simulations with various values of rubble thicknesses and friction coefficients was performed.

The article is ordered as follows. First the bases of the modelling technique are discussed: FEM–DEM is briefly described and derivation of contact forces is presented. Then actual simulations of punch through tests are described and an example simulation is presented. This is followed by the presentation of results: force displacement graphs, shear strength, deformation patterns and the failure process of the rubble achieved from simulations are presented. The last part includes discussion on results and comparisons to earlier research on rubble properties.

2. Combined finite–discrete element method

Modelling of the ridge keel was performed by using the combined finite–discrete element method (FEM–DEM). A thorough description of the FEM–DEM can be found e.g. from Munjiza et al. (1995) and Munjiza (2004). In FEM–DEM, discrete elements are meshed into finite elements. In the method presented here, each ice block is modelled with a discrete element divided into six tetrahedron shaped finite elements. Contact forces are solved finite element by finite element. The total contact force acting on a discrete element is thus achieved by superposition of forces acting on its finite elements. The finite elements and thus the ice blocks in simulations were assumed to be rigid.

The main tasks to be executed during one time step of a FEM–DEM simulation are: (a) neighbor search, (b) contact resolution analysis and (c) update of block positions for the next time step. In phase (a), blocks in the vicinity of each other, and possibly interacting on a given time step, are found without referring to their exact geometry but only to their extent. This is done to reduce the computational burden introduced by phase (b). The algorithm used in phase (a) was the NBS-algorithm by Munjiza and Andrews (1998) with some modifications. In the computationally intensive phase (b), contact geometries between contacting finite elements are solved and contact forces are determined. An algorithm for solving contact geometry with tetrahedron shaped finite elements has been presented by Munjiza (2004). In phase (c), blocks are moved into new positions by applying Newton's laws. An explicit time stepping scheme is used to update block positions.

2.1. Contact forces

Contact forces were derived using penalty function and potential contact force method (Munjiza and Andrews, 2000; Munjiza, 2004). In the potential contact force method, a potential φ with continuous first partial derivatives with respect to spatial coordinates is defined in every point P of each finite element volume Ω. Further, $\varphi=\varphi(P)$ should vanish on finite element boundaries Γ for smooth collision response. Hence

$$\varphi(P)>0, \quad P\in\Omega \quad \wedge \quad \varphi(P)=0, \quad P\in\Gamma. \tag{1}$$

When tetrahedron shaped finite elements are used, an obvious choice for $\varphi(P)$ is the volume coordinates of a tetrahedron.

The contact force $d\mathbf{f}_\varphi$ applied to an infinitesimal volume element $d\Omega_o$ penetrating into φ is determined from the gradient of φ as (Fig. 2a)

$$\frac{d\mathbf{f}_\varphi(P)}{d\Omega_o} = -s\nabla\varphi(P), \tag{2}$$

where s is a positive constant penalty term. The negative sign is due to repulsive nature of the contact force. The contact force $\mathbf{f}_\varphi$ due to $\varphi(P)$

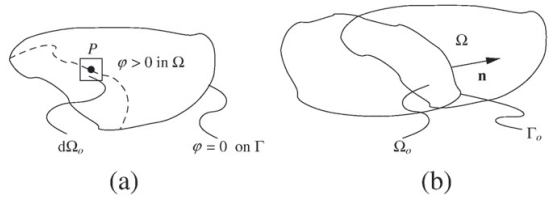

Fig. 2. (a) An infinitesimal volume element $d\Omega_o$ at point P penetrating into a finite element with volume Ω and (b) the overlap volume Ω_o of two elements.

is determined by integration over the overlap volume Ω_o of two colliding elements. The integral is reduced into computationally more efficient form by generalized Gauss's theorem

$$\mathbf{f}_\varphi = -s\int_{\Omega_o}\nabla\varphi(P)\ \mathrm{d}\Omega = -s\int_{\Gamma_o}\varphi(P)\mathbf{n}\ \mathrm{d}\Gamma, \tag{3}$$

where $\mathbf{n}$ is the unit outer normal of Γ_o (Fig. 2b). From the previous equation it can be seen that the distributed load acting on overlapping volume elements due to φ becomes reduced to a force acting on a single point on Γ_o. As finite elements used in simulations presented in this work are tetrahedron shaped, Γ_o is a triangular surface and forces on finite element nodes are applied according to the surface coordinates of Γ_o.

The inelasticity in collisions is modelled by using viscous damping relative to the rate of change in overlap volume. The viscous component of the normal force $\mathbf{f}_v$ is defined as

$$\mathbf{f}_v = c\Gamma_0(\mathbf{v}_r\cdot\mathbf{n})\mathbf{n}, \tag{4}$$

where $\mathbf{v}_r\cdot\mathbf{n}$ is the normal component of the relative velocity of the contacting discrete elements at the point of application of $\mathbf{f}_\varphi$ and c is the viscous damping constant.

As no tensile forces between colliding blocks are allowed, the total contact force $\mathbf{f}_c$ should always act on the direction of $-\mathbf{n}$ in contacts. This is achieved by the following condition:

$$\mathbf{f}_c = \begin{cases} 0, & \text{if } |\mathbf{f}_\varphi| - |\mathbf{f}_v| < 0 \\ \mathbf{f}_\varphi - \mathbf{f}_v & \text{else.} \end{cases} \tag{5}$$

Dissipation due to sliding friction is modelled by using dynamic Coulomb friction. Frictional force $\mathbf{f}_\mu$ is solved from

$$\mathbf{f}_\mu = -\mu|\mathbf{f}_c|\frac{\mathbf{v}_r - \mathbf{v}_r\cdot\mathbf{n}}{|\mathbf{v}_r - \mathbf{v}_r\cdot\mathbf{n}|}, \tag{6}$$

where μ is the friction coefficient and $\mathbf{v}_t - \mathbf{v}_t\cdot\mathbf{n}$ is the tangential component of the relative velocity of contacting blocks at the point of contact.

2.2. External forces

No hydrodynamic forces were modelled as simulations were run only with low puncher velocities ($\dot{\delta}$ = 25…50 mm s^{-1}). Due to this, ice block velocities were expected to be low. The only external force acting on blocks was buoyant force. As all ice blocks of the rubble are below the water surface throughout simulations, the buoyant force for a block j is given by the equation

$$\mathbf{f}_{b,j} = (\rho_w - \rho_i)V_j g\mathbf{j} \tag{7}$$

where ρ_w and ρ_i are respectively mass densities of the water and ice, V_j is the volume of the block j and g is the gravitational acceleration. The direction $\mathbf{j}$ of the buoyant force is parallel to the direction of positive y-axis (see Fig. 3 for the coordinate frame). For each block, $\mathbf{f}_{b,j}$ is applied to its centroid.

Table 1
Main parameters used in simulations

	Parameter	Symbol	Unit	Value
General	Number of ice blocks			1740…4600
	Number of finite elements			10200…27600
Contact	Penalty term	s		$1.0\cdot10^6$…$1.0\cdot10^8$
	Damping constant	c	Ns m^{-3}	$5.0\cdot104$…$8.0\cdot10^4$
	Time step	Δt	s	$1.0\cdot10^{-4}$…$2.0\cdot10^{-4}$
Ice blocks	Length		m	0.3…1.5
	Width		m	0.3…1.5
	Thickness		m	0.2
	Mass density	ρ_i	kg m^{-3}	920
	Friction coefficient	μ		0.05…0.6
Water	Mass density	ρ_w	kg m^{-3}	1010
Keel	Keel depth	h	m	2.1…3.48
	Rubble porosity	η_r		0.34…0.51
Indentor	Diameter	d	m	4.7
	Velocity	$\dot{\delta}$	mm s^{-1}	25…50
Pool	Length		m	20
	Width		m	20

3. Simulations

In the following, FEM–DEM simulations of punch through tests are described and an illustrative example of a simulation is given. In these simulations, the full scale tests conducted by Heinonen and Määttänen (2000) are modelled (Fig. 1). Table 1 gives the main parameters used in the simulations and Fig. 3 shows the coordinate frame. Origin is located at the top of the rubble and y-axis aligns with the center line of the indentor. It was observed that the ice rubble behaviour followed cylindrical symmetry around the indentor, and hence cylindrical coordinates are used. Fig. 4 illustrates a typical initial configuration of a simulation. A sketch of the initial configuration is shown in Fig. 5, where the indentor platen is colored dark gray, the ice rubble is light gray and the ice sheet covering the rubble is gray.

To generate an ice rubble, blocks with random translational and rotational velocities were released underwater. The initial velocities were altered to create different initial rubble configurations. After releasing, the blocks were allowed to float to form the initial rubble mass. At this phase the indentor was kept in the position δ_0 measured from the bottom of the top ice sheet (Fig. 5). To ensure a quasi static ice rubble for an actual punch-through simulation, each initial simulation was allowed to advance to a point where the kinetic energy of ice blocks became dissipated due to frictional and viscous damping forces. To model the full scale experiments (Fig. 1), the pool was covered with a discrete element representing the ice sheet on top of the rubble (not shown in Fig. 4). Simulations were performed using 1740…4600 blocks depending on the initial keel thickness. Total

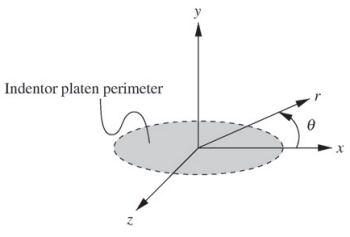

Fig. 3. Cylindrical coordinate frame (r, θ, y) used in the text. Plane y = 0 is located at the top of the rubble, y-axis aligns with the center line of the indentor, and x-axis is parallel with one of the pool walls, see Fig. 4.

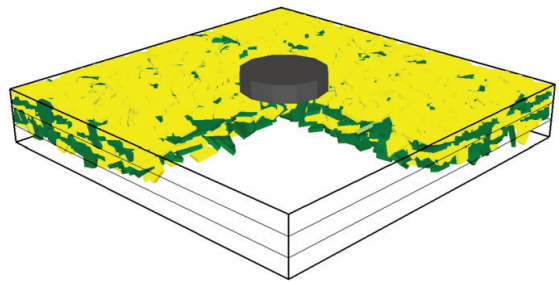

Fig. 4. Typical initial configuration of the keel. Ice blocks at one quarter of the pool and the ice sheet covering the pool are not shown in the figure.

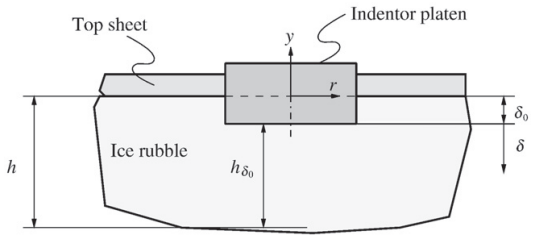

Fig. 5. Two dimensional sketch of the simulation. Initial displacement of the indentor is δ_0, indentor displacement is δ, average rubble thickness is h as in Fig. 1, and average rubble thickness under the indentor is h_{δ_0}.

amount of finite elements in simulations thus varied between 10,200…27,600.

Dimensions for individual ice blocks were chosen after field measurements in the Baltic Sea by Kankaanpää (1997) and Heinonen and Määttänen (2000, 2001b). Following the measurements by Heinonen and Määttänen (2000), the thickness of the ice blocks was chosen to be 0.2 m. The average side length to thickness ratio 5.5 measured by Kankaanpää (1997) was used, and blocks with side lengths 1.1 m ± 0.4 m were generated using random number generator. By doing this, block sizes similar to those observed by Heinonen and Määttänen (2000) were achieved. In addition, elongated blocks and small blocks were added to the rubble. Also for comparison, simulations with homogenous rubble consisting of blocks with equal dimensions 0.2 m × 1.1 m × 1.1 m were performed. Puncher diameter d was 4.7 m.

In the punch through phase of the simulation, the indentor was moved downwards into the ice rubble as presented in snapshots of Fig. 6. In the snapshots, ice blocks with centroids initially at $z < 0$ are shown and the camera is looking into the direction of negative z-axis (Fig. 3). Blocks are colored with two different colors according to the initial y-coordinate of their centroids. The force F applied by the rubble on the indentor into the direction of y-axis was monitored. The indentor was accelerated into the target velocity with acceleration 25 mm s^{-2}. Then, for example, the indentor velocity $\dot{\delta} = 50$ mm s^{-1} was reached after indentor displacement $\delta = 50$ mm. Contacts between the indentor and blocks and between the pool walls and blocks were frictionless.

The pool size was chosen after gauging the force exerted on walls by the rubble to avoid boundaries of the pool to have an effect on measured force values and deformation pattern of the rubble. Results presented here are from simulations with pool size 20 m × 20 m. Simulations with larger pools were also performed, but using a larger pool did not change the results.

The sensitivity of the simulation results to the penalty term s, damping constant c (Eqs. (3) and (4)) and time step Δt was tested with various initial configurations. Note that s is not a material parameter. The values of s and c affect the block contacts but also the computing time. If s and c are increased, the value of the time step Δt has to be decreased in order to maintain numerical stability, and if Δt is decreased, running times of simulations increase. Values of $s = 1.0 \cdot 10^6 \ldots 1.0 \cdot 10^8$, $c = 5.0 \cdot 10^4 \ldots 8.0 \cdot 10^4$ Ns m^{-3} and $\Delta t = 1.0 \cdot 10^{-4} \ldots 2.0 \cdot 10^{-4}$ s were tested.

4. Results

In this section, simulation results are presented in the scope of the discussion of the following section. In total 47 simulations were performed. Table 1 gives the main simulation parameters.

4.1. Porosity

Porosities of the generated piles were measured before the punch through phase of simulations. The value of η_r varied between 0.34…0.51 with the average value of $\bar{\eta}_r = 0.44$. The rubble porosity η_r was

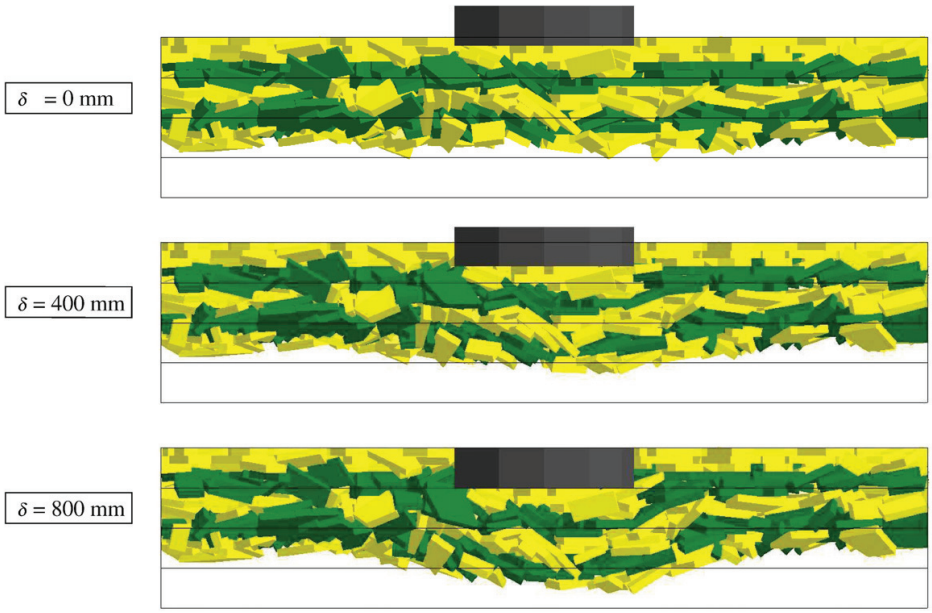

Fig. 6. An illustrative example of a simulation of a punch-through test with various values of puncher displacement δ. The initial displacement δ_0 of the indentor in the simulation presented in snapshots was 200 mm.

defined as the volume of cavities V_c divided by the volume of the ice rubble V_r

$$\eta_r = \frac{V_c}{V_r} = \frac{V_r - V_i}{V_r}, \tag{8}$$

where V_i is the total volume of ice blocks in a simulation. The volume of the rubble V_r was defined using the average keel thickness h (Fig. 5), side lengths a of the pool, indentor diameter d and initial indentor displacement δ_0:

$$V_r = ha^2 - \pi d\delta_0. \tag{9}$$

V_i was readily available after determination of ice block mass properties, but h had to be defined afterwards by post processing data from simulations.

4.2. Force displacement records and maximum force

Fig. 7 shows typical $F(\delta)$ graphs from three different simulations. These graphs are f rom simulations with the same initial configuration but with different values of μ. Also in Fig. 7, F_{MAX} for each simulation is presented.

From Fig. 7 it is noticed that initially $F(\delta)$ increases rapidly. Then increase in F is slower until F reaches an approximately constant level with some oscillations. These oscillations typically had an amplitude up to 3 kN and were of two different types. Some were due to individual ice blocks colliding with the indentor in which case they were rapid and quickly decaying transients. The smoother oscillations are interpreted as relative motion of ice blocks leading to release of shape interlocking and redistribution of inter-particle forces within the rubble. F_{MAX} was defined as the average of F on its approximately constant level. Typically F reached F_{MAX} with $\delta \approx 150\ldots200$ mm depending on the rubble thickness and block properties. In Fig. 8, F_{MAX} from 47 simulations with various values of μ are plotted against the initial keel depth h_{δ_0} (Fig. 5). In the figure, F_{MAX} for simulations with homogeneous ice rubble consisting of ice blocks with equal dimensions are presented with circled markers.

In addition to simulation results, F_{MAX} from the field experiment #1/2001 by Heinonen and Määttänen (2001b) is shown in Fig. 8. This experiment provides a good comparison for the simulations, as the experiment was conducted on an unconsolidated keel obtained by first conducting a punch through test, and then conducting another test where the indentor was moved down into the same rubble again. It can be assumed, that after the first punch the freeze bonds were broken and the keel behaved as an unconsolidated rubble. From the experimental result, the buoyant force F_b of the indentor, i.e. ice cylinder formed by cutting through the consolidated layer, was subtracted (Fig. 1). F_b is given by

$$F_b = (\rho_w - \rho_i) g\pi \left(\frac{d}{2}\right)^2 h_{\text{cut}} \tag{10}$$

and has a value 14.7 kN for test 1/2001. During the experiment, some wooden planks and a steel plate were put on top of the indentor. These could have caused some pre-stress on the rubble and also could have affected the value of the buoyant force, but were, however, not taken into account here.

From Fig. 8 it can be seen, that F_{MAX} increases with the increase in h_{δ_0} as could be expected. Also it is seen, that F_{MAX} increases as μ is increased and h_{δ_0} is constant. Some simulations, e.g. such as presented in Fig. 7, were run using the same initial configuration but different values if μ. In all of these simulations, increase in μ caused increase in F_{MAX}. Multiple simulation runs were performed with approximately same h_{δ_0} but with different initial configurations. Hence, it is seen that F_{MAX} is not strongly sensitive to the initial configuration (when configuration is random).

Also in Fig. 8, the buoyant force F_α of a rubble cone with top diameter d, height h_{δ_0}, slant height l, and bottom diameter defined by angle α (see Fig. 1) is shown for three different values of α. F_α is achieved from

$$F_\alpha = (\rho_w - \rho_i)(1 - \overline{\eta}_r) V_\alpha g \tag{11}$$

where $\overline{\eta}_r$ is as presented in Section 4.1 and V_α is the volume of the rubble cone given by

$$V_\alpha = \frac{\pi h_{\delta_0}}{3}\left[\left(\frac{d}{2}\right)^2 + \frac{d}{2}\left(\frac{d}{2} + h_{\delta_0}\tan\alpha\right) + \left(\frac{d}{2} + h_{\delta_0}\tan\alpha\right)^2\right]. \tag{12}$$

4.3. Shear strength

A value for rubble shear strength can be obtained by assuming a cylindrical failure surface (α=0, Fig. 1) defined by the perimeter of indentor platen and rubble thickness (Croasdale et al., 2001;

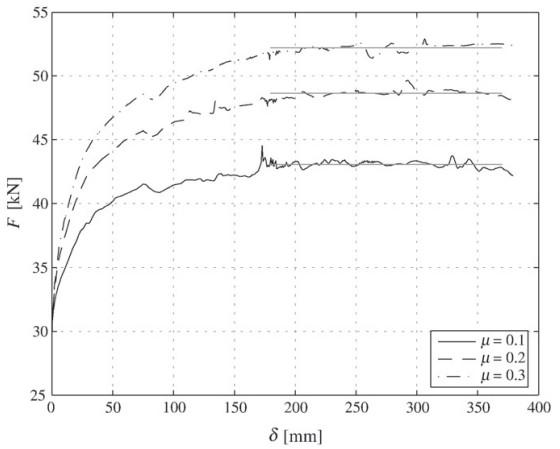

Fig. 7. $F(\delta)$ graphs for three simulation runs with different μ. F_{MAX} is defined in Section 4.2 and is shown with a gray line for each simulation.

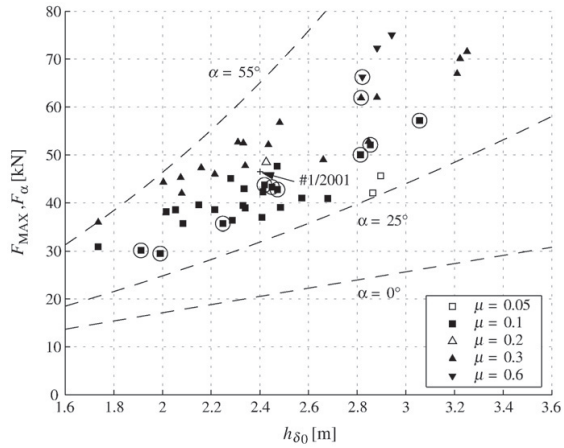

Fig. 8. The maximum force F_{MAX} as a function of h_{δ_0} from simulations and experiment #1/2001. F_α is buoyant force defined by Eq. (11). See text for details.

Heinonen, 2004). If h_{δ_0} is used for rubble thickness, a shear strength τ_{δ_0} is obtained as

$$\tau_{\delta_0} = \frac{F_{MAX}}{\pi d h_{\delta_0}}, \quad (13)$$

where F_{MAX} does not include the buoyant force due to the consolidated layer. Fig. 9 shows τ_{δ_0} from simulations and experiment 1/2001 (Heinonen and Määttänen, 2001b). τ_{δ_0} in the figure is from the same 47 simulations from which F_{MAX} was obtained and shown in Fig. 8. Markers for simulations with homogeneous rubble consisting of equal block sizes are circled in the figure. It is seen that τ_{δ_0} increases with the increase of μ. Table 2 gives the average values of τ_{δ_0} for different friction coefficients.

5. Discussion

5.1. Simulations

The indentor used in simulations was circular and the deformation pattern was noticed to follow cylindrical symmetry. To reduce the size of simulations, it would seem like an obvious choice to use cylindrical symmetry and only model a quarter of the pool with quarter of the indentor placed in the corner. After visual observations on the packing and orientation of ice blocks close to pool walls and from the $F(\delta)$ graphs in test cases using symmetry, it was noticed that results were not representative for the whole rubble. Hence, the whole pool was modelled.

The sensitivity of the simulations to penalty term value s was done by running fifteen simulation runs with five different initial configurations with penalty term values $1.0\cdot10^6$, $1.0\cdot10^7$ and $1.0\cdot10^8$. It was found out that the τ_{δ_0} values achieved from the simulations increased on average by 7% when s was increased from $1.0\cdot10^6$ to $1.0\cdot10^7$. Further, the increase in τ_δ was 3.5% when penalty term was increased from $1.0\cdot10^7$ to $1.0\cdot10^8$.

On the other hand, it was observed that the value of τ_{δ_0} between different initial configurations with same value of s commonly varied up to 20%. Further, from the average values of τ_{δ_0} shown in Table 2, it can be seen that the average value of τ_{δ_0} increased 23% as the value of μ was increased from 0.1 to 0.3 and 16% as the value of μ was increased from 0.3 to 0.6. Hence, it was concluded that $s = 1.0\cdot10^7$ used in the simulations was high enough.

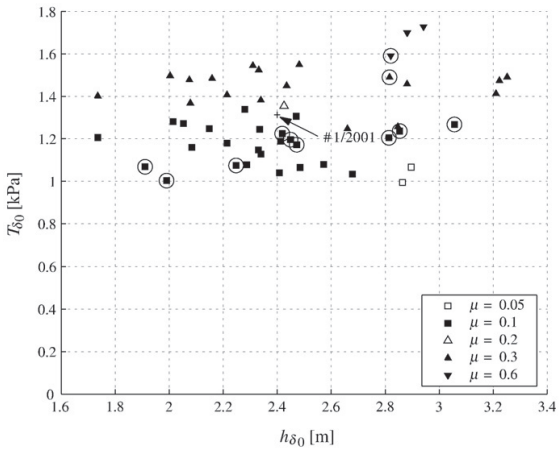

Fig. 9. The shear strength τ_{δ_0} with various values of μ plotted against h_{δ_0} from simulations and experiment #1/2001 using the assumption of cylindrical failure. See text for details.

Table 2
Average values $\bar{\tau}_{\delta_0}$ of τ_{δ_0} (Eq. (13)) for different friction coefficients μ

μ	$\bar{\tau}_{\delta_0}$ [kPa]	N
0.1	1.17	26
0.3	1.44	18
0.6	1.67	3

N is the number of data points.

The observed insensitivity of simulation results to the variation of penalty term s and damping constant c (Section 3) can be discussed using a simple rheological model illustrated in Fig. 10. In the model, blocks are connected to each other with springs (stiffness k) and viscous dampers (damping coefficient ν). Also a buoyant force is applied on blocks. The response of this simple system with contact properties k and ν is analogous to the simulated ice rubble with contact properties s and c. Clearly, if block 1 is forced to displace into direction y with constant $\dot{y}$, the total force applied to block 1 by the rest of the system reaches constant level at some y due to buoyancy applied on the blocks. It is also clear, that this constant force value is independent of k and ν.

Value of Δt was chosen to maintain the numerical stability of the simulation. Further, it was observed that the variation of c within the tested limits ($5.0\cdot10^4$ …$8.0\cdot10^4$ Ns m^{-3}) did not affect τ_{δ_0}.

5.2. Shear strength

The shear strength $\tau_{\delta 0}$ for simulated piles was given in Fig. 9 and the average shear strength $\bar{\tau}_{\delta_0}$ for different values of μ in Table 2. Using the same definition for rubble shear strength as here (Eq. (13)), Leppäranta and Hakala (1992) reported shear strength values 1.7… 4 kPa, Heinonen (2004) reported values 1.3…18 kPa, and Croasdale et al. (2001) reported values 6…12.8 kPa. The values from simulations are in the low end when compared to experimental data, but this is expected, as no cohesive bonding between ice blocks was modelled. In fact, the effect of the rubble consolidation, i.e. cohesive bonding between the ice blocks, on rubble strength can be estimated by comparing the simulated results with the highest experimental values.

It should be noticed, that Azarnejad and Brown (2001) have used a different definition for rubble shear strength than here. In their terminology, a load-time record consists of an ascending part, peak load F_{MAX}, descending part, and residual load F_R. If inertial effects are ignored, Azarnejad and Brown (2001) define shear strength as $\tau = (F_{MAX} - FR)/A$, where A is area. The residual load F_R is the average load for a period at the end of an experiment when the load remains virtually constant. In the simulations reported here, no such constant residual load following a peak load was observed. If a simulation was continued long enough, the force started to descend after F_{MAX}, but did not level into a constant value. Further, if a residual load would still be defined, in all the simulations $F_{MAX} \approx F_R$ (Fig. 9), and using the definition of Azarnejad and Brown (2001) would result into very small or vanishing shear strength.

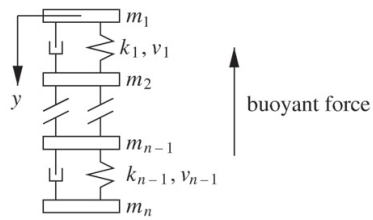

Fig. 10. A simplified rheological model of blocks with masses m_i connected in series with springs (stiffness k) and dampers (damping coefficient ν).

Fig. 11 shows τ_{δ_0} as a function of porosity η_r for different values of μ. Also the shear strength measured by Heinonen and Määttänen (2001b) is shown in the figure. This full scale test result is presented with a dashed gray line, as porosity η_r for the experiment is not known. As before, markers for simul ations with homogeneous rubble consisting of blocks with equal dimensions are circled in the figure. Regression analysis with least squares method using linear fit was performed for results with μ=0.1 and μ=0.3 and the lines are shown in Fig. 11. The analysis yielded polynomials $-1.4\eta_r+1.8$ (with coefficient of determination R^2=0.45) and $-0.6\eta_r+1.7$ (R^2=0.15) for μ=0.1 and μ=0.3, respectively, when all the simulation results were taken into account. The regression analysis was also performed separately for results with rubble consisting of various block shapes. This analysis yielded to similar results as above, but the dependency was slightly clearer as $R2$=0.66 for μ=0.1 and $R2$=0.16 for μ=0.3. When porosity η_r of a rubble pile increases, the amount of contacting and sliding surfaces within the pile decreases. Hence, it could be expected that the shear strength of a pile would be inversely proportional to η_r. The trend achieved from the regression analysis seems to support this even though the values of R^2 are low. It should be noticed that the effect of the porosity in real ice rubble may be different from simulations. As hydrodynamic forcesare not modelled, the possible effect of pore pressure is not modelled. Further, the porosity affects the freeze bonding of the rubble (Ettema and Urroz, 1989).

Porosity η_r of the simulated ice rubble was 0.34…0.51 with average $\bar{\eta}_r$=0.46. These values are higher than those measured in-situ, but not exceptional (Kankaanpää, 1997; Heinonen and Määttänen, 2000, 2001b; Heinonen, 2004). As an example, during winter 1999, Heinonen (2004) measured values η_r=0.31…0.46 with average $\bar{\eta}_r$=0.38. The high porosity of the simulated rubble is probably due to the rigid and unbreakable ice blocks used in the simulations. In full-scale ice blocks collide with each other and corners of the blocks break off allowing a denser packing than in the simulations, where such small scale ice failures were not modelled. It is also possible that the different rubble generation processes in-situ and in the simulations lead to differences in porosity.

5.3. Failure process

The ice rubble failure process during a punch through test was studied through a detailed analysis of one simulation. The parameters of the simulation used for this purpose are given in Table 3. Fig. 12 illustrates the rubble displacement v_r in the negative y-direction at the beginning of a simulation. Deformation of the rubble was observed to follow cylindrical symmetry, and thus the displacement shown is the average displacement of surface points on ice blocks with equal r-coordinates but with different values of θ around the axis r=0. As v_r is the displacement of a surface point, v_r is affected by both translation and rotation. Fig. 13 shows a sequence of displacement profiles at the later stages of this simulation. Snapshots and $F(\delta)$-graph of this simulation are given in Figs. 14 and 15, respectively.

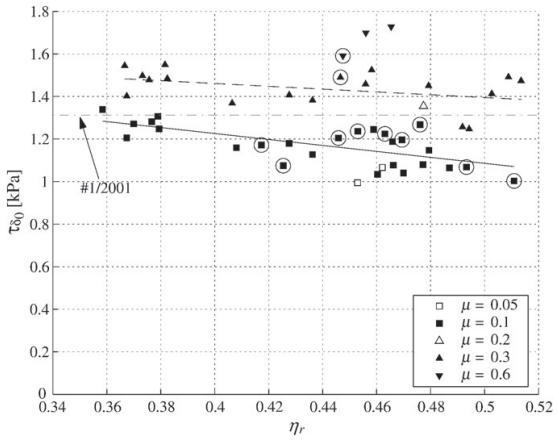

Fig. 11. The shear strength τ_{δ_0} (Eq. (13)) from simulations and from experiment #1/2001 (dashed gray line). η_r is rubble porosity. The solid and dashed black regression lines are for μ=0.1 and μ=0.3, respectively. See also text for details.

Table 3
Parameters of a simulation

d [m]	h [m]	$\dot{\delta}$ [mm/s]	μ	η_r [%]	F_{MAX} [kN]
4.7	2.0	50	0.3	0.37	44.3

The results of this simulation are shown in Figs. 12 to 15. d is indentor diameter, h is keel thickness, $\dot{\delta}$ is indentor velocity, μ is friction coefficient, η_r is rubble porosity and F_{MAX} is the maximum force as defined in Section 4.2.

As shown in Fig. 12, already in the very beginning of the simulation the indentor displacement δ is transmitted to the bottom of the rubble close to the center line of the indentor. Ice blocks moving with the indentor at the indentor velocity ($v_r \approx \delta$) form a mass with the shape of a truncated cone. The base of the cone aligns with the bottom of the indentor and the cone opens upwards. This behaviour was observed to occur irrespective of the initial indentor displacement δ_0. Values ranging through 30…300 mm were studied. Hence, it can be concluded that it was not due to pre-arranged structure of the rubble due to δ_0 during the rubble generation phase. Also from the experimental data by Heinonen and Määttänen (2001b) it was seen that the bottom of an unconsolidated keel started its movement already with small values of δ.

The initially forming mass of rubble moving at the indentor velocity is spreading horizontally as the punch through test proceeds. The shape of the rubble moving at $v_r \approx \delta$ changes from an upward opening cone into a cylinder with diameter of the indentor as illustrated in Fig. 13. In other words, the rubble within a cylinder defined by the indentor perimeter is moving down as one block and the internal structure of it seems to be virtually undisturbed. This behaviour is typical to simulations with high friction coefficient, whereas with low friction coefficient, the rubble is compacting, as will be described below. From the snapshots of Fig. 14 with δ>100 mm, it is seen that a zone of rotating ice blocks is formed around the rubble with $v_r \approx \delta$. In addition to the rotation of ice blocks, typically shape locking was also detected to occur on this zone. Figs. 12 and 13 show further that ice blocks affected by the indentor, i.e. ice blocks with displacement v_r>0.1δ, form the shape of a downward opening cone. This cone is also well illustrated in the snapshots of Fig. 14. The rubble outside of this downward opening cone remains undisturbed.

The rubble deformation can be further studied by analysing the displacement of keel bottom in the negative y-direction. Fig. 16 presents average keel bottom displacements $\bar{v}_b$ from simulations with 8 different initial configurations for two different friction coefficients, μ=0.1 and μ=0.3. The simulations with μ=0.3 show

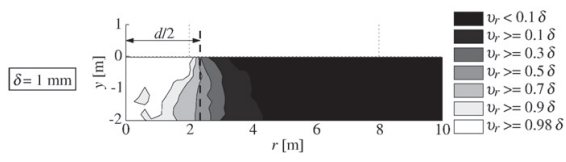

Fig. 12. Contour plot of average rubble displacement in the beginning of a simulation when indentor displacement δ=1 mm. v_r is displacement of a surface point of an ice block in the negative y-direction. r and y are coordinates. The displacements are presented in the initial configuration of the rubble.

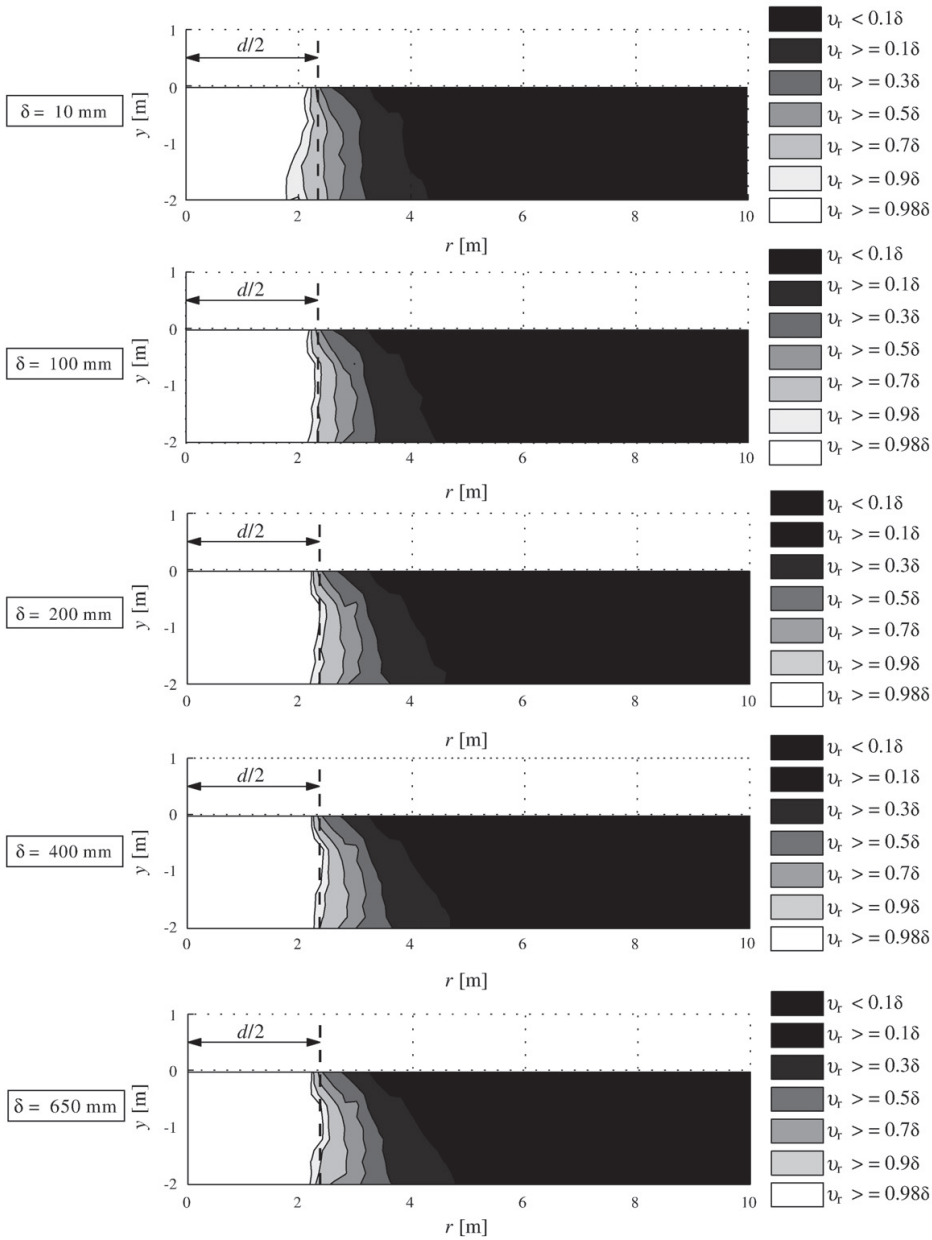

Fig. 13. Contour plots of average rubble displacements. v_r is displacement of a surface point of an ice block in the negative y-direction and δ is indentor displacement. r and y are coordinates. The displacements are presented in the initial configuration of the rubble. Snapshots of this simulation are shown in Fig. 14, $F(\delta)$-graph in Fig. 15, and the parameters in Table 3.

larger displacement in the bottom of the keel than simulations with μ=0.1. The same observation can be reached by studying compaction of the rubble, defined here as the ratio $(\bar{v}_b(\delta)-\delta)/h_{\delta_0}$. Fig. 17 illustrates the keel compaction for the same simulation data as used in Fig. 16. These simulations show that compaction is negligible up to δ=700 mm when μ=0.3, but when μ=0.1, compaction initiates at $\delta\approx$200 mm. It should be noticed, that in both cases the maximum force F_{MAX} is reached with approximately the same value of δ.

As described earlier and illustrated in Fig. 13, no unique shear plane that could be defined by an angle α (see Fig. 1) was detected in the simulations. Rather, a zone with displacement gradient was observed. However, an approximation for a shear plane angle α_t can be defined by using a threshold value v_t for the displacement v_b at a point (r_t, y_t) in the keel bottom. Here the threshold value v_t=100 mm was chosen to be half of the block thickness. It can be observed from the bottom profiles shown in Fig. 16 that the condition $v_b(r_t, y_t)=v_t$ defines

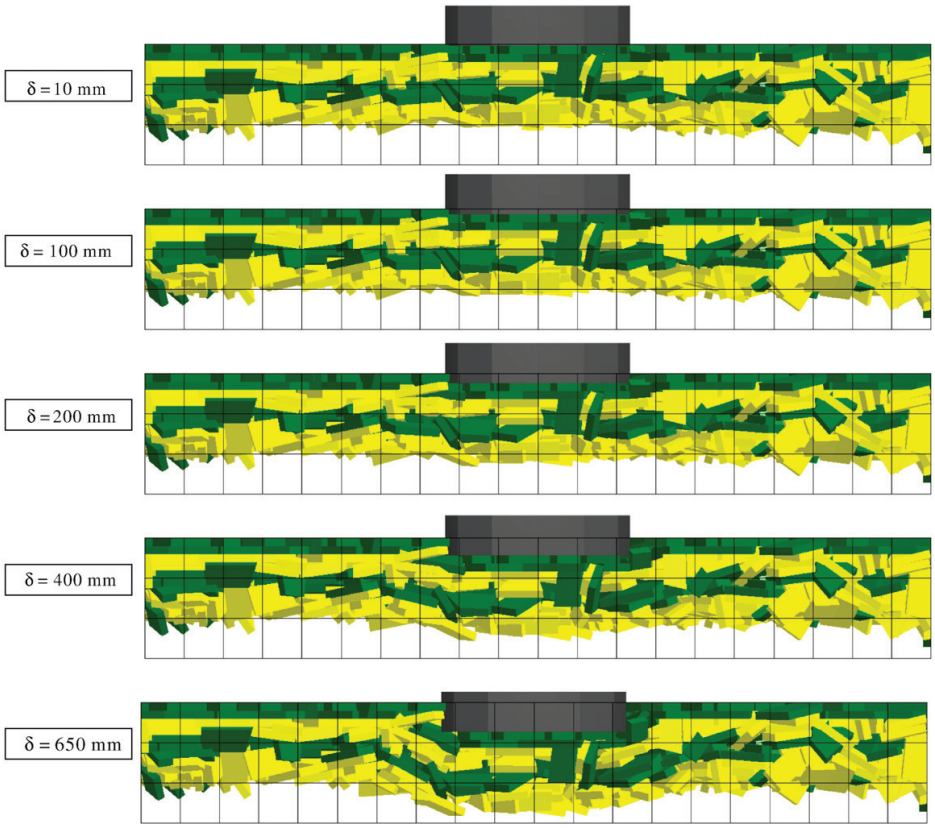

Fig. 14. Snapshots of a simulation. δ is the indentor displacement. Ice blocks with centroids initially at $z<0$ are shown and the camera is looking into the direction of negative z-axis (see Fig. 3). The blocks are colored according to the initial y-coordinate of their centroids. The $F(\delta)$-graph of this simulation is presented in Fig. 15, the displacement profiles in Fig. 13, and the parameters in Table 3. The grid size in the snapshots is 1 × 1 m.

unambiguously a single point, and between that point and the axis $r=0$, $v_b(r_t, y_t) \geq v_t$. The positive direction of α_t is defined to be away from the indentor center line as presented for α in Fig. 1, and hence α_t is defined as

$$\alpha_t(\delta) = \arctan\left(\frac{r_t - d/2}{|y_t|}\right) \tag{14}$$

where d is the indentor diameter. Fig. 18 shows $\alpha_t(\delta)$-graphs for the same simulation data as used in Figs. 16 and 17.

The results shown in Fig. 18 are in agreement with the visual observations, where deformation in the keel bottom initiated close to the center line of the indentor (Fig. 12). This is indicated by values $\alpha_t<0$ in the beginning of the indentor motion. With $\delta<150$ mm, the rate $\partial\alpha_t/\partial\delta$ is large. This corresponds to the observation on the change in the angle defining the zone of the displaced rubble (Figs. 12 and 13). As mentioned earlier, also the rate $\partial F/\partial\delta$ has large value with small δ. This could suggest that the high $\partial F/\partial\delta$ is related to the change in the deformation pattern on the start-up of a punch through test. As δ increases further, $\partial\alpha_t/\partial\delta$ decreases. Angle α_t is increasing slowly as $\delta>400$ mm corresponding to the approximately constant zone of moving rubble. It should be noticed that with high δ values, sliding of ice blocks away from indentor center line due to generated bulge may cause some increase in α_t.

The above approximation of failure plane angle α_t reaches values of 35…45° with the indentor stroke lengths used. Lemee and Brown (2002) conducted a series of laboratory scale punch through tests in plane strain conditions. For unconsolidated rubble consisting ice blocks with dimensions small compared to the indentor size, they

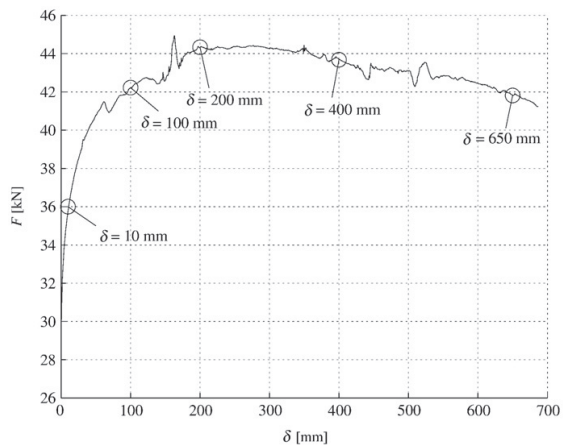

Fig. 15. $F(\delta)$-graph of a simulation. Snapshots of this simulation are shown in Fig. 14, displacement profiles in Fig. 13, and the parameters in Table 3.

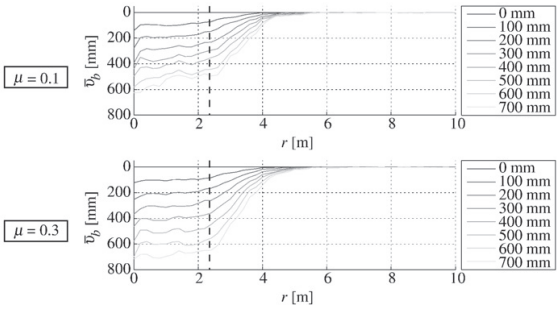

Fig. 16. Average profiles of keel bottom displacements $\bar{v}_b$ with various values of indentor displacement δ (shown in the legend) with μ=0.1 and μ=0.3 with same initial configurations. The displacements were averaged from eight simulations for each μ. The perimeter of the indentor is shown with dashed line.

measured a failure angle of 38.8° on average. In another series of laboratory scale punch-through tests in plane strain conditions, Jensen et al. (2001) observed a failure angle of approximately 40°.

The values of α_t given in Fig. 18 can further be related with the indentation force results shown in Fig. 8. In that figure, the buoyant force F_α of rubble mass with the shape of a truncated cone defined by α is presented for three different values of α. Comparison of the results given in Figs. 8 and 18 suggests that in the final stages of the simulated punch through tests, a major part of the force on the indentor is due to buoyancy of the ice rubble.

Based on the simulation results described above, in a punch through test three main processes can be identified: (1) a volume of rubble with the shape of an upward opening cone forms under the indentor, moves with the indentor ($v_r \approx \delta$), and spreads out into a cylindrical plug, (2) ice blocks around this conical / cylindrical core rotate (or shape lock and rotate) causing the zone of displaced rubble to spread horizontally, i.e. the angle α_t defining a downward opening cone containing moving rubble grows, until (3) α_t reaches an approximately constant value and the rubble within the cone defined by αt moves downwards. Processes (1) and (2) occur at least partly simultaneously.

The different processes can be identified also in the $F(\delta)$-graph presented in Fig. 15. The slope $\partial F/\partial\delta$ has a large value at the start of the indentor motion. This large value is due to inertial and frictional forces during formation of the conical/cylindrical core of rubble with displacement $v_r \approx \delta$. The simulations suggest further, that F_{MAX} is

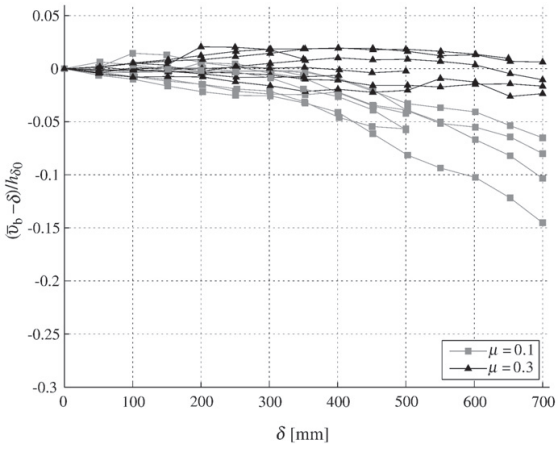

Fig. 17. Compaction of ice rubble for the same simulation data as used in Fig. 16.

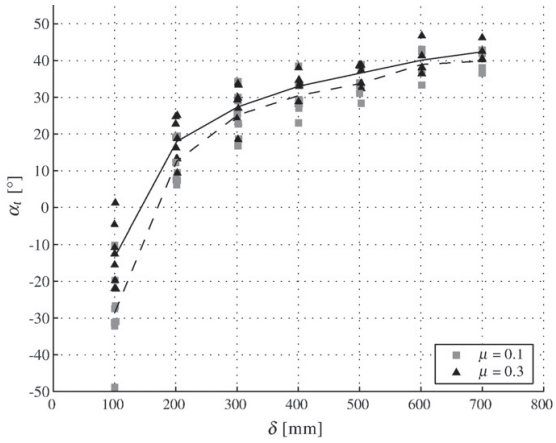

Fig. 18. Angle α_t as a function of δ. Displacement threshold v_t = 100 mm in the rubble bottom was used. The average values of α_t for μ=0.3 and μ=0.1 are shown with solid and dashed line, respectively.

reached when the rubble deformation pattern is fully developed. This fully developed pattern includes a core moving with the indentor and a shear zone where the displacement of ice blocks gradually changes from $v_r \approx \delta$ to $v_r \approx 0$. In the final stage the load decreases as, due to buoyancy, ice blocks at the rubble bottom start to slide away from the bulge generated by the displaced rubble. In other words, the load starts to decrease when ice blocks start to move away from the indentor center line in the horizontal direction. The onset of this final stage is affected by friction coefficient and rubble thickness.

Although the simulations were performed with full scale dimensions and material properties, comparisons on failure process between laboratory scale experiments and simulation results were made. This was done, as the possibility to observe the failure process during full scale experiments is limited and more data from laboratory experiments is available. Azarnejad et al. (1999) and Azarnejad and Brown (2001) conducted a series of laboratory punch through tests where they varied the indentor velocity, the time for aging of the ice rubble and ice rubble thickness. In tests with deformation rates $\dot{\delta}$<40 mm s^{-1} they observed a failure process similar with the current simulations: a rectangular, or in some cases trapezoidal, plug of undisturbed ice moved down with the indentor. Around the plug, within a zone of two to three blocks, rotation of ice blocks occurred, but the rubble outside of the zone of rotating blocks remained undisturbed. However, with higher deformation rates, the failure process became more obscure.

Typical $F(\delta)$ records from laboratory experiments are different from the ones obtained from simulations. The laboratory data show fast build-up of F to a peak with subsequent decrease into a constant value (Azarnejad and Brown, 2001; Lemee and Brown, 2002). As illustrated in Fig. 15, in simulations the rate $\partial F/\partial\delta$ is initially high but no sharp force peak is observed. This difference can be explained by assuming that the resistance of ice rubble under deformation can be divided in two main components: the cohesive resistance of the rubble due to freeze bonding and the frictional resistance. According to Azarnejad and Brown (2001), the cohesive resistance is observed in $F(\delta)$ records before frictional resistance as δ is increasing. As no cohesion was modelled, this phenomenon is absent in the simulation results.

Finally, the $F(\delta)$ records achieved from the simulations were compared to results from field experiments by Heinonen and Määttänen (2001b). Similarly with the laboratory test results, the $F(\delta)$ records from full scale experiments show usually a large peak load at the very beginning of a test. This peak is due to breaking of

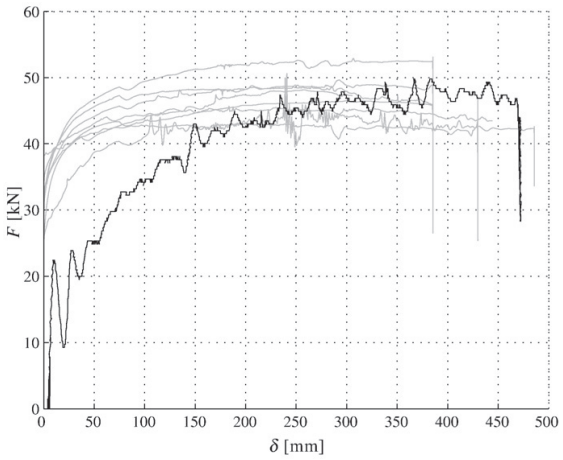

Fig. 19. The $F(\delta)$-graph from the full-scale experiments conducted by Heinonen and Määttänen (2001b) (black) and simulation runs with h_{δ_0}=2.21…2.85 m (gray).

freeze bonding. Therefore, as freeze bonding (cohesion) was not modelled, the simulation results are compared with experimental results obtained with unconsolidated rubble as explained in Section 4.2. Fig. 19 shows the $F(\delta)$ record from the experiment #1/2001 and the $F(\delta)$ records from simulations with h_{δ_0}=2.21…2.85 m. The maximum force values from the experiments and simulations are similar, but the initial $\partial F/\partial\delta$ slopes are different. The simulated system is stiffer. This difference in stiffness comes from two sources. While the ice blocks in the simulations are rigid and did not break, the ice blocks in the field experiments experience edge crushing and other local failure modes effecting the rubble stiffness. Another difference is rigidity of the test fixture. In the simulations, the indentor was rigid and moved with a constant velocity, while in the field experiments, the rigidity of the loading rig was finite. This difference in stiffnesses affects also the dynamic response of the systems. Experimental data includes more vibration type force fluctuations than seen on the data from the simulations.

6. Conclusions

Ridge keel punch through tests on an unconsolidated rubble pile were simulated in 3D. Combined FEM–DEM with rigid discrete elements was used in the modelling. The simulated rubble consisted of loose discrete elements representing ice blocks. Block sizes were based on in-situ observations. Simulations were run with various values of keel thicknesses and friction coefficients. Force F acting on the indentor and rubble displacements v_r were measured. The measured data was used to derive shear strength of the rubble and to study the failure process.

Simulation results were verified through comparison with full-scale and laboratory experiments. The indentation force values achieved from simulations were in the range of full-scale test results for unconsolidated rubble. The simulated failure process was observed to be similar to laboratory experiments.

In simulations, the indentor force F initially increased with displacement δ. After reaching maximum value F_{MAX}, F remained approximately constant. This constant force value was used to derive shear strength for the rubble. No clear peak force value with subsequent drop to a constant value was observed. Such a peak force is typical to experimental data and it is believed that it is missing from the simulation results because no cohesive forces were modelled.

Following previous studies, the shear strength of the rubble was calculated by assuming cylindrical failure. The rubble shear strength values obtained from simulations were in the low end when compared to experimental data. Again, this is expected as no cohesive bonding between the blocks was modelled. Friction was noticed to effect the shear strength. Increase in the value of friction coefficient was seen to lead to an increase in shear strength.

The value of friction coefficient was also observed to affect the compaction of the rubble. Compaction was seen to be negligible with the now used indentor stroke lengths when friction coefficient 0.3 was used, whereas with value 0.1, compaction was clearly observed.

Failure process of the rubble was analyzed. No unique shear plane was detected in simulations. Instead, a shear zone within which $0 \le v_r \le \delta$ was observed to form during the indentor motion. The location and the shape of the shear zone was observed not to be constant during the indentor motion. Further, the indentor displacement δ was observed to become transmitted through the rubble already at the very beginning of the indentor motion. Keel bottom displacements were observed to first occur close to the center line of the indentor. These observations of the rubble deformation during a punch through test can be captured into three stage process: (1) a volume of rubble with a shape of an upward opening cone with $v_r \approx \delta$ forms under the indentor and spreads out into cylindrical plug, (2) blocks around this core rotate causing the zone of displaced rubble to spread horizontally into a downward opening cone, until (3) angle defining the downward opening cone reaches an approximately constant value and the rubble within it moves downwards. The increase of F to value F_{MAX} was observed to be related to the first two stages of this process.

Acknowledgments

The financial support from the Ministry of Education of Finland through the National Graduate School in Engineering Mechanics and from the Academy of Finland is gratefully acknowledged.

References

Azarnejad, A., Brown, T.G., 2001. Ice rubble behaviour in punch tests. ASCE Journal of Cold Regions Engineering 15 (3), 135–153.
Azarnejad, A., Frederking, R., Brown, T.G., 1999. Ice rubble strength from plane strain punch tests. Proc. of the 18th Int. Conf. on Onshore Mechanics and Arctic Engineering, OMAE, 1–9. St. Johns, Canada.
Bruneau, S., Crocker, G., McKenna, R., Croasdale, K., Metge, M., Ritch, R., Weaver, J., 1998. Development of techniques for measuring in situ ice rubble shear strength. Ice in Surface Waters, Proc. Of the 14th International Symposium on Ice, IAHR, vol. 2, pp. 1001–1007. Potsdam, New York, USA.
Croasdale, K.R., Bruneau, S., Christian, D., Crocker, G., English, J., Metge, M., Ritch, R., 2001. In-situ measurements of the strength of first-year ice ridge keels. Proceedings of the 16th International Conference on Port and Ocean Engineering under Arctic Conditions, POAC'01, vol. 3, pp. 1445–1454. Ottawa, Ontario, Canada.
Cundall, P., Strack, O., 1979. A discrete numerical model for granular assemblies. Geotechnique 29, 47–65.
Ettema, R., Urroz, E., 1989. On internal friction and cohesion in unconsolidated ice rubble. Cold Regions Science and Technology 16 (3), 237–247.
Heinonen, J. (2004) Constitutive modeling of ice rubble in first-year ridge keel. Doctoral Thesis, TKK. VTT Publications 536. Espoo, Finland, 2004, 142 p, ISSN 1235-0621.
Heinonen, J., Määttänen, M., 2000. Ridge loading experiments, field experiments in winter 2000. LOLEIF Progress Report No. 10, TKK. 40 pp.
Heinonen, J., Määttänen, M., 2001a. Full-scale testing of ridge keel mechanical properties in loleif project. Proceedings of the 16th International Conference on Port and Ocean Engineering under Arctic Conditions, POAC'01, vol. 3, pp. 1435–1444. Ottawa, Ontario, Canada.
Heinonen, J., Määttänen, M., 2001b. Ridge keel mechanical properties — testing. field experiments in winter 2001. STRICE-report, TKK. 39 pp.
Hopkins, M., 1992. Numerical simulation of systems of multitudinous polygonal blocks. Technical Report 92–22. Cold Regions Research and Engineering Laboratory, CRREL. 69 pp.
Hopkins, M., 1998. Four stages of pressure ridging. Journal of Geophysical Research 103 (C10), 21,883–21,891.
Hopkins, M., Tuhkuri, J., Lensu, M., 1999. Rafting and ridging of thin ice sheets. Journal of Geophysical Research 104 (C6), 13605–13613.
Jensen, A., Løset, S., Høyland, K.V., Liferov, P., Heinonen, J., Evers, K.-U., Määttänen, M., 2001. Physical modelling of first-year ice ridges — part II: mechanical properties.

Proceedings of the 16th International Conference on Port and Ocean Engineering under Arctic Conditions, POAC'01, vol. 3, pp. 1493–1502. Ottawa, Ontario, Canada.
Kankaanpää, P., 1997. Distribution, morphology and structure of sea ice pressure ridges in the baltic sea. Fennia 175 (2), 139–240 ISSN 0015-0010.
Lemee, E., Brown, T., 2002. Small-scale plane strain punch tests. Ice in the Environment: Proc. of the 16th IAHR International Symposium on Ice, vol. 2, pp. 1–7. Dunedin, New Zealand.
Leppäranta, M., Hakala, R., 1992. The structure and strength of first-year ice ridges in the baltic sea. Cold Regions Science and Technology 20 (3), 295–311.
Liferov, P., 2005. Ice rubble behaviour and strength: Part II. Modelling. Cold Regions Science and Technology 41 (2), 153–163.
Liferov, P., Bonnemaire, B., 2005. Ice rubble behaviour and strength: Part I. review of testing and interpretation of results. Cold Regions Science and Technology 41 (2), 135–151.
Liferov, P., Jensen, A., Høyland, K., 2002. On analysis of punch tests on ice rubble. Proceedings of the 16th International Symposium on Ice, vol. 2, pp. 101–110. Dunedin, New Zealand.
Liferov, P., Jensen, A., Høyland, K., 2003. 3D finite element analysis of laboratory punch tests on ice rubble. Proceedings of the 16th International Symposium on Ice, vol. 2, pp. 611–621. Trondheim, Norway.
Munjiza, A., 2004. The combined finite–discrete element method. John Wiley & Sons Ltd., Chichester, England.
Munjiza, A., Andrews, K., 1998. NBS contact detection algorithm for bodies of similar size. International Journal for Numerical Methods in Engineering 43 (1), 131–149.
Munjiza, A., Andrews, K., 2000. Penalty function method for combined finite–discrete element systems comprising large number of separate bodies. International Journal for Numerical Methods in Engineering 49 (11), 1377–1396.
Munjiza, A., Owen, D., Bićanić, N., 1995. A combined finite–discrete element method in transient dynamics of fracturing solids. Engineering Computations 12, 145–174.
Paavilainen, J., Tuhkuri, J., Polojärvi, A., 2006. Discrete element simulation of ice pile-up against an inclined structure. Proceedings of the 18th International Symposium on Ice, IAHR, vol. 2, pp. 177–184. Sapporo, Japan.
Tuhkuri, J., Polojärvi, A., 2005. Effect of particle shape in 2D ridge keel deformation simulations. Proceedings of the 18th International Conference on Port and Ocean Engineering under Arctic Conditions, POAC'05, vol. 2, pp. 939–948. Potsdam, New York, USA.